

See discussions, stats, and author profiles for this publication at: <https://www.researchgate.net/publication/26702845>

Detailed Evaluation of the Geometric and Electronic Structures of One-Electron Oxidized Group 10 (Ni, Pd, and Pt) Metal(II)–(Disalicylidene)diamine Complexes

ARTICLE *in* INORGANIC CHEMISTRY · JULY 2009

Impact Factor: 4.76 · DOI: 10.1021/ic901003q · Source: PubMed

CITATIONS

51

READS

33

3 AUTHORS, INCLUDING:



Yuichi Shimazaki

Ibaraki University

75 PUBLICATIONS 1,548 CITATIONS

SEE PROFILE



Tim Storr

Simon Fraser University

60 PUBLICATIONS 1,392 CITATIONS

SEE PROFILE

Published in final edited form as:

Inorg Chem. 2009 September 7; 48(17): 8383–8392. doi:10.1021/ic901003q.

Detailed Evaluation of the Geometric and Electronic Structures of One-electron Oxidized Group 10 (Ni, Pd, and Pt) Metal(II)-(Disalicylidene)diamine Complexes

Yuichi Shimazaki^a, T. Daniel P. Stack^b, and Tim Storr^c

Yuichi Shimazaki: yshima@mx.ibaraki.ac.jp; T. Daniel P. Stack: ; Tim Storr: tim_storr@sfu.ca

^aCollege of Science, Ibaraki University, Bunkyo, Mito 310-8512, Japan

^bDepartment of Chemistry, Stanford University, Stanford, CA, 94305, U. S. A.

^cDepartment of Chemistry, Simon Fraser University, Burnaby, BC, Canada

Abstract

The geometric and electronic structures of a series of one-electron oxidized group 10 metal salens (Ni, Pd, Pt) have been investigated in solution and in the solid state. Ni (**1**) and Pd (**2**) complexes of the tetradentate salen ligand *N,N'*-bis(3,5-di-*tert*-butylsalicylidene)-1,2-cyclohexanediamine (H₂Salcn) have been examined along with the Pt (**3**) complex of the salen ligand *N,N'*-bis(3,5-di-*tert*-butylsalicylidene)-1,2-ethylenediamine (H₂Salen). All three oxidized compounds exist as ligand radical species in solution and in the solid state. The solid state structures of [**1**]⁺ and [**3**]⁺ exhibit a symmetric coordination sphere contraction relative to the neutral forms. By contrast, the coordination sphere of the Pd derivative [**2**]⁺ exhibits a pronounced asymmetry in the solid state. In solution, the oxidized derivatives display intense low-energy NIR transitions consistent with their classification as ligand radical compounds. Interestingly, the degree of communication between the phenolate moieties depends strongly on the central metal ion, within the Ni, Pd, and Pt series. Electrochemical measurements and UV-Vis-NIR spectroscopy, in conjunction with DFT calculations provide insights into the degree of delocalization of the one-electron hole in these systems. The Pd complex [**2**]⁺ is the least delocalized and is best described as a borderline Class II/III intervalence complex based on the Robin-Day classification system. The Ni [**1**]⁺ and Pt [**3**]⁺ analogues are Class III (fully delocalized) intervalence compounds. Delocalization is dependent on the electronic coupling between the redox-active phenolate ligands, mediated by overlap between the formally filled metal d_{xz} orbital and the appropriate ligand molecular orbital. The degree of coupling increases in the order Pd < Ni < Pt for the one-electron oxidized group 10 metal salens.

1. Introduction

The interplay of redox-active transition metal ions and pro-radical ligands in metalloenzyme sites is an area of substantial research interest,¹⁻⁴ and in an effort to better understand this interaction numerous transition-metal complexes with organic radical ligands have been studied.⁵⁻⁹ Examples include transition-metal complexes with non-innocent ligands such as dioxolenes,⁶ dithiolenes,^{10,11} *o*-phenylenediamines,¹²⁻¹⁵ and salens.¹⁶⁻²² Building on this

Correspondence to: Yuichi Shimazaki, yshima@mx.ibaraki.ac.jp; Tim Storr, tim_storr@sfu.ca.

Supporting information Available: Complete ref. ⁶²; experimental details including the CIF files for **2**, [**2**]⁺ SbF₆⁻, and [**3**]⁺ SbF₆⁻; CV data for **1-3** at 298 K; TD-DFT spectra for [**1-3**]⁺; UV-Vis-NIR spectra for [**1-3**]⁺ in different solvents; computational details including TD-DFT excitation energies and oscillator strengths; orbital constituent analysis; and the Cartesian coordinates for geometry-optimized **1-3** and [**1-3**]⁺. This material is available free of charge via the Internet at <http://pubs.acs.org>.

work, small-molecule systems have been designed that incorporate ligand non-innocence into catalyst design.²³⁻³⁵ This is of particular relevance to metal salen, many of which have proven to be versatile catalysts for organic transformations.³⁶⁻⁴⁰

Depending on the relative energies of the redox-active orbitals, metal complexes with non-innocent ligands exist in two limiting descriptions, either a metal-ligand radical ($M^{n+}(L^{\bullet})$) or a high valent metal ($M^{(n+1)+}(L^-)$) complex. Oxidized metal salen complexes are known to exist in either form, and the factors that control the locus of oxidation in these complexes are being pursued currently.¹⁶⁻²² Sterically demanding *ortho* and *para* substituents on the phenolates are critical for the stabilization of the oxidized metal salen complexes, which are prone to rapid polymerization via radical coupling even at low temperatures.⁴¹⁻⁴⁵ The one-electron oxidized NiSalcn complex **[1]**⁺ (Figure 1) exists in a ligand radical form in the solid state and in solution,^{19,46} yet the presence of coordinating anions and/or solvent, shifts the locus of oxidation to the nickel center, forming a Ni(III) complex.^{16-19,44,46} The Pd (**2**) and Pt (**3**) analogues also form ligand radical species upon oxidation.²¹ The oxidized Pd and Pt salen complexes do not undergo a shift in the locus of oxidation in the presence of exogenous ligands, consistent with the large ligand field stabilization energy associated with d⁸ metal ions of the second and third row transition metals.

Oxidation of the copper derivative CuSalcn results in a high-valent, diamagnetic Cu(III) species in the solid state.²² In solution however, a temperature-dependent equilibrium is thought to exist between a Cu(III) and a ferromagnetically-coupled Cu(II)-ligand radical form, indicating nearly isoenergetic species. The shift in the locus of oxidation from the ligand for **[1]**⁺ to the metal for **[CuSalcn]**⁺ matches the trend for the monoanionic Ni and Cu dithiolenes.^{9-11,47} For **1**, the redox-active orbitals of the ligand are positioned at higher energy in comparison to the d-orbital manifold, resulting in ligand non-innocence upon oxidation to **[1]**⁺. For CuSalcn, occupancy of a higher energy ($d_{x^2-y^2}$) metal-centered orbital results in metal-based oxidation. These studies suitably demonstrate how the relative ordering of redox-active orbitals in a complex affects the locus of oxidation.

Experimental analysis of **[1]**⁺ demonstrates that the two identical redox-active phenolate ligands are highly coupled, and that the unpaired electron is extensively delocalized.¹⁹ This complex was classified as a Robin-Day⁴⁸ Class III (fully delocalized) intervalence complex. The Robin-Day classification system was originally developed to analyze the electronic coupling in metal-centered mixed valence systems,⁴⁹ whereby an organic linker mediated the coupling between the two mixed valence metal ions. Hush provided a theoretical model for intervalence charge transfer,⁵⁰ and the continued study of intervalence compounds has greatly improved the understanding of electron transfer in these systems.⁵¹⁻⁵⁵ Comparatively less is known about ligand-based mixed valent systems, in which electronic coupling is mediated by a metal ion bridge.^{11,15,19,20,56-63} Our present work investigates the influence of different bridging metal atoms (Ni, Pd, Pt) on the electronic coupling in one-electron oxidized salen complexes.

We have recently reported the synthesis and characterization of a series of one-electron oxidized Group 10 metal (Ni, Pd, Pt) salen complexes.²¹ Analysis of the one-electron oxidized forms indicated that the degree of electronic coupling between the phenolate moieties is dependent on the central metal ion, within the Ni, Pd, and Pt series. The Pd analogue was determined to be the most 'localized' ligand radical of this series by resonance Raman and X-ray photoelectron spectroscopy (XPS) studies. The Pt derivative, while still a ligand radical species, exhibited significant high-valent metal character on the basis of EPR, XPS, and X-ray absorption spectroscopy (XAS) measurements.

We now describe in greater detail the geometric and electronic structure of the one-electron oxidized Group 10 metal (Ni, Pd, Pt) salen complexes. Solid state characterization of the oxidized Pd and Pt derivatives, in conjunction with UV-Vis-NIR spectroscopy, electrochemistry, and DFT calculations allows for evaluation of the influence of the central metal ion on the electronic structure of these mixed valence systems.

2. Experimental Section

2.1. Materials and Methods

All the chemicals used were of the highest grade available and were further purified whenever necessary.⁶⁴ *N,N'*-bis(3,5-di-*tert*-butylsalicylidene)ethylenediamine (= **H₂Salen**) and *N,N'*-bis(3,5-di-*tert*-butylsalicylidene)-1,2-cyclohexanediamine (= **H₂Salcn**) (Figure 1) and their group 10 metal(II) complexes were prepared according to the literature.^{19,21} [Ni(**Salcn**)]SbF₆ [**1**]⁺ was synthesized by a previously reported method.¹⁹ Electronic spectra were obtained with a Shimadzu UV-3101PC spectrophotometer. Cyclic voltammetry (CV) was performed using a BAS CV-40 potentiometer, a Ag wire reference electrode, platinum disk working electrode, and a Pt wire counter electrode with 0.1 M Bu₄NClO₄ solutions in CH₂Cl₂. Ferrocene was used as an internal standard.

2.2. Synthesis of [Pd(**Salcn**)]SbF₆ [**2**]⁺

To a solution of Pd**Salcn** (**2**) (0.065 g, 0.1 mmol) in CH₂Cl₂ (5 mL) was added AgSbF₆ (0.034 g, 0.1 mmol) in CH₂Cl₂ (5 mL) under N₂. The resulting solution was filtered and toluene (5 mL) was added to the filtrate. The solution was kept standing at less than 0 °C for 24 h under N₂ atmosphere to afford green crystals of [**2**]⁺. Elemental analysis (%) calcd for [**2**]⁺ (C₃₆H₅₂N₂O₂PdSbF₆): C, 48.75; H, 5.91; N, 3.16. Found: C, 48.49; H, 5.89; N, 3.19.

2.3. Synthesis of [Pt(**Salen**)]SbF₆ [**3**]⁺

This complex was prepared in a manner similar to that for [**2**]⁺. Elemental analysis (%) calcd for [**3**]⁺ (C₃₂H₄₆N₂O₂PtSbF₆): C, 41.71; H, 5.03; N 3.04. Found: C, 41.77; H, 5.07; N, 3.03.

2.4. X-ray Structure Determination

X-ray experiments were carried out for well-shaped single crystals of complexes of [**2**], [**2**]⁺ and [**3**]⁺ on a Rigaku RAXIS imaging plate area detector with graphite monochromated Mo K α radiation (λ = 0.71073 Å) at -150 °C. The crystals were mounted on a glass fiber. In order to determine the cell constants and orientation matrix, three oscillation photographs were taken for each frame with an oscillation angle of 3° and an exposure time of 3 min. Reflection data were corrected for both Lorentz and polarization effects. The structures were solved by the heavy-atom method and refined anisotropically for non-hydrogen atoms by full-matrix least-squares calculations. Each refinement was continued until all shifts were smaller than one third of the standard deviations of the parameters involved. Atomic scattering factors and anomalous dispersion terms were taken from the literature.⁶⁵ All hydrogen atoms were located at the calculated positions and were assigned a fixed displacement and constrained to an ideal geometry with C–H = 0.95 Å. The thermal parameters of calculated hydrogen atoms were related to those of their parent atoms by $U(H) = 1.2U_{eq}(C)$. All the calculations were performed using the TEXSAN program package.⁶⁶ A summary of the crystal data and experimental parameters for the structure determinations are given in Table 1.

2.5. Calculations

Geometry optimizations were performed using the Gaussian 03 program (Revision C.02),⁶⁷ the PBE0 functional,⁶⁸ the SDDAll basis set^{69,70} (Ni, Pd, Pt), and the 6-31G(d) basis set (C, H, N, O). The PBE0 functional was chosen due to a recent report highlighting the ability of

this functional to accurately predict coordination sphere geometries of a series of Pt pincer complexes.⁷¹ The **Salen** ligand (ethyl backbone) was used in the calculations for consistency; use of the cyclohexyl backbone had a negligible effect on the calculated coordination sphere bond lengths, or electronic properties. Single-point calculations were performed using the PBE0 functional, the SDDAll basis set (Ni, Pd, Pt), and the TZVP basis set of Ahlrichs⁷² (C, H, N, O). AOMIX⁷³⁻⁷⁵ was used for determining atomic orbital compositions employing Mulliken Population Analysis. The intensities of the 30 lowest-energy electronic transitions were calculated by TD-DFT^{76,77} with the same functional/basis set combination employed for the single-point calculations, and a polarized continuum model (PCM) for CH₂Cl₂ (dielectric $\epsilon = 8.94$).⁷⁸⁻⁸¹

3. Results and Analysis

3.1. Synthesis and Solid State Characterization

Ni(II), Pd(II) and Pt(II) complexes of the tetradentate salen ligands **NiSalen** (**1**), **PdSalen** (**2**), and **PtSalen** (**3**) were synthesized by previously reported methods.^{19,21} The X-ray structure of **2** is displayed in Figure 2. These group 10 metal complexes were oxidized by one-electron with AgSbF₆ in CH₂Cl₂/toluene under an inert atmosphere,¹⁹ affording single crystals suitable for X-ray structural analysis of the one-electron oxidized Pd (Figure 3) and Pt complexes (Figure 4).

Single crystals of the Pd complex [**2**]⁺ were isolated from a reaction mixture stored at ca. 0 °C for 24 h. The absorption and EPR spectra of this crystalline material dissolved in CH₂Cl₂ were essentially the same as that of [**2**]⁺ prepared by direct oxidation of **2**. The EPR spectrum of [**2**]⁺ is invariant to temperature change in the range of 77–300 K.²¹ The X-ray structures of **2** (Figure 2) and [**2**]⁺ (Figure 3) each exhibit a slightly distorted square planar geometry. The coordination sphere bond lengths of the neutral and one-electron oxidized Ni, Pd, and Pt compounds are shown in Table 2, allowing for a comparison of the changes to coordination sphere metrical parameters for the three derivatives upon oxidation.

Oxidation of **2** to [**2**]⁺ results in slightly longer Pd–O bond lengths on average (+0.01 Å), while the Pd–N bond lengths shorten by 0.01 Å. The contraction in Pd–N bond lengths is similar to that observed for the M–N bond lengths of the Ni and Pt derivatives upon oxidation (Table 2). The greater coordination sphere asymmetry in [**2**]⁺ (1.963 Å and 2.003 Å for the Pd–O bonds) as compared to the Ni and Pt derivatives, suggests asymmetric radical distribution, which is further manifest in the two C–O bonds (1.317 Å and 1.263 Å). The correlation of the shorter C–O and longer Pd–O bonds is consistent with a quinoid bonding pattern. This matches with the structures of other reported phenoxyl radical complexes,⁸²⁻⁸⁴ indicating a greater degree of localization of the ligand radical for [**2**]⁺ to one side of the molecule. A lengthening of the ring *ortho* C–C bonds (average values of two phenolate moieties in [**2**]⁺: 1.471 Å and 1.435 Å) further evidences this quinoid bonding pattern (Figure 5).

The slightly distorted square-planar geometry of the one-electron oxidized Pt complex [**3**]⁺ (Figure 4) is similar to that of the neutral precursor **3**, with both the Pt–O and Pt–N bond lengths of [**3**]⁺ shorter by ca. 0.02 Å (Table 2). The phenolate/phenoxyl C–O bond distances of [**3**]⁺ (1.309 and 1.299 Å) are slightly shorter in comparison to the same bonds in **3** (1.325 Å). The similarity between the two Pt–O and two C–O bond lengths in [**3**]⁺, support a more symmetrical distribution of the radical character in comparison to [**2**]⁺ (Figure 5).

While the Ni and Pt derivatives exhibit a clear coordination sphere contraction in both M–O and M–N bond lengths upon oxidation, the Pd complex becomes asymmetric, indicating a greater degree of localization of the ligand radical on one of the phenolate rings in the oxidized form. This solid state structural data, in combination with the experimental results reported

previously,²¹ prompted us to further investigate the electronic structure of these one-electron oxidized group 10 (Ni, Pd, and Pt) metal salen complexes.

3.2. Theoretical Characterization

Density Functional Theory (DFT) calculations on the group 10 metal salen complexes and one-electron oxidized forms well reproduce the coordination sphere bond lengths of the respective compounds (Table 2). At the PBE0⁶⁸/SDDAll^{69,70} (Ni, Pd, Pt) / 6-31G(d) (C, H, O, N) level of theory, the predicted coordination sphere bond distances by geometry optimization match those of the X-ray structures by $\pm 0.04 \text{ \AA}$ (Table 2). Optimization effectively results in a C_2 -symmetric structure in all cases. The effective core potential SDDAll basis set was chosen for the metal atoms in order to be consistent; the TZVP⁷² and 6-31G(d) basis sets are only parameterized to Kr, and thus cannot be used for Pd and Pt. The calculated coordination sphere bond lengths for the one-electron oxidized Ni, Pd, and Pt complexes exhibit a small contraction in comparison to the neutral forms (Table 2). The predicted coordination sphere contraction upon oxidation matches the experimental data for both the Ni and Pt complexes, as well as the partial contraction (Pd-N bonds) for the Pd derivative. The optimized structure for $[2]^+$ fails to predict the asymmetric Pd-O bonds observed experimentally, a common result due to the tendency of DFT to favor delocalized, higher symmetry structures.⁸⁵ The computations predict that the oxidation of the group 10 metal salens occurs through removal of an electron from a predominantly ligand-based π^* orbital (vide infra). Extended charge decomposition analysis (ECDA)⁷³ for **1** and $[1]^+$ suggests that coordination sphere contraction is due to an approximately equal increase in both ligand-to-metal ($L \rightarrow M$) donation and metal-to-ligand ($M \rightarrow L$) back-donation upon oxidation.²² This is in contrast to the substantial increase in donation ($L \rightarrow Cu$) for the oxidized metal derivative $[Cu(III)Salen]^+$, in comparison to the neutral analogue $Cu(II)Salen$, in which the hole created upon oxidation is localized on the copper center.²²

Calculations support a delocalized ligand radical electronic structure for $[1]^+$, $[2]^+$, and $[3]^+$. The calculated spin density for $[3]^+$ (Figure 6) shows a typical pattern for a phenoxyl radical on each ring, with significant positive spin population at the O (0.16), *Cortho* (0.10), and *Cpara* (0.14) positions. While the shortened C-O bonds in the X-ray structure of $[3]^+$ are consistent with a quinoid bonding pattern, the pattern is not manifest in the rings, likely because of delocalization of the radical over both ring systems. A similar bonding pattern to that of $[3]^+$ is observed in both $[1]^+$ and $[2]^+$. The calculated spin density at the metal center for the oxidized group 10 metal salens follows the trend Pd (8 %) < Ni (12 %) < Pt (17 %), showing a non-negligible contribution from the metal d_{xz} orbital (Figure 6), in accordance with previously collected experimental data.²¹

3.3. Electrochemistry

The degree of electronic coupling between the two redox-active phenolates in complexes $[1]^+$, $[2]^+$, and $[3]^+$, and the extent of electronic delocalization, was probed by cyclic voltammetry. The comproportionation constant (Equations 1 and 2) assesses the stability of the mono-oxidized complex, relative to the fully reduced and doubly-oxidized forms. The comproportionation constant K_c (Equation 2) can be estimated from the difference between the first and second oxidation potentials (ΔE_{ox}) via Equation 3.⁵⁵



$$K_c = \frac{[ML\bullet]^2}{[ML][ML\bullet\bullet]} \quad (2)$$

$$K_c = \exp\left(\frac{\Delta E_{ox} F}{RT}\right) \quad (3)$$

The first oxidation is reversible for **1-3** by cyclic voltammetry at 298 K. While the second oxidation is quasi-reversible for the Ni derivative, oxidation to the doubly-oxidized species is irreversible for both the Pd and Pt complexes at this temperature (Figure S1). At 230 K, the doubly-oxidized derivatives are much more stable on the electrochemical timescale (Figure 7).

At this temperature two reversible redox processes are observable for **1**, **2**, and **3**; the potentials versus the ferrocenium/ferrocene couple (Fc^+/Fc) are reported in Table 3. The two oxidation waves can be attributed to ligand-based oxidation processes leading to a mono- and presumably a bis-phenoxyl radical species.¹⁸ The order of the first redox potential ($E_{1/2}^1$) is Pt < Ni < Pd, and is opposite to the order of the second redox potential ($E_{1/2}^2$) Pd < Ni < Pt. The values of ΔE_{ox} and K_c for the three derivatives (Table 3) demonstrate that the Pt species exhibits the largest coupling between the two redox-active phenolates, followed by the Ni derivative, and finally the Pd species. These results highlight the influence of the metal ion bridge in mediating the coupling between the two phenolate ligands in the Ni, Pd and Pt series.

3.4. Absorption Spectroscopy

Only the one-electron oxidized complexes, not the neutral derivatives, exhibit intense low-energy bands in the NIR (Figure 8). Of particular interest is the intense NIR band for $[1]^+$ at 4700 cm^{-1} ($\epsilon = 21500\text{ M}^{-1}\text{ cm}^{-1}$), which is assigned as a ligand-to-ligand charge transfer band (LLCT) on the basis of experimental and theoretical analysis (Table 4, Figure 8a).^{19,46} Oxidation of the Pd derivative **2** to $[2]^+$ results in the appearance of NIR bands (Figure 8b), but with significantly lower intensities compared to the NIR transitions for the Ni analogue. Spin quantitation of the EPR spectrum of $[2]^+$ demonstrates that the NIR intensity differences between the oxidized Ni and Pd complexes is not a result of decomposition in CH_2Cl_2 solution. Oxidation of the Pt complex **3** to $[3]^+$ also results in the appearance of NIR transitions (Figure 8c). The NIR bands for $[3]^+$ are the most intense in the series (Table 4), at 10300 cm^{-1} ($\epsilon = 9400\text{ M}^{-1}\text{ cm}^{-1}$), and 5450 cm^{-1} ($\epsilon = 32600\text{ M}^{-1}\text{ cm}^{-1}$).

We have previously examined the shape and intensity of the NIR band of $[1]^+$ to aid in the assignment of this species as a Class III mixed valence complex.¹⁹ Class III systems exhibit transitions that are characteristically intense ($\epsilon_{\text{max}} \geq 5000\text{ M}^{-1}\text{ cm}^{-1}$), solvent independent and exhibit narrow bandwidths ($\Delta\nu_{1/2} \leq 2000\text{ cm}^{-1}$).⁵⁵ This analysis is now extended to the Pd and Pt derivatives to provide further insight into the role of the metal ion in facilitating the electronic coupling between the two redox-active phenolate ligands.

$$\Delta\nu_{\text{HTL}} = \sqrt{16\ln 2 RT \nu_{\text{max}}} \quad (4)$$

The experimental bandwidths ($\Delta\nu_{1/2}$) for the oxidized complexes are significantly less than the predicted minimum bandwidth ($\Delta\nu_{\text{HTL}}$) in the high-temperature limit (Table 5), consistent with the description of these complexes as borderline Class II/III or Class III mixed valence

complexes. These results reflect the inability of Marcus-Hush theory to predict IVCT bandshape at the Class II/III borderline.⁵⁴ Band shape analysis of $[2]^+$ (Table 5) suggests that this derivative is the least delocalized system of the series, in agreement with our previous results,²¹ and the data presented herein.

The sensitivity of the IVCT transition to variation in solvent polarity is a useful criterion for distinguishing between localized and delocalized mixed valence complexes.^{51,55} The IVCT band(s) of delocalized mixed valence complexes (Class III) are insensitive to solvent changes, whereas localized systems (Class II) are generally not. The latter is due to the dipole change associated with charge transfer, resulting in solvent reorganization.

The solvent dependence of the low energy NIR band for the one-electron oxidized group 10 metal salens was probed in toluene, CH_2Cl_2 , and CH_3CN (Table 6), providing a range in solvent polarity. Solvent-induced decomposition and/or solvent binding limited the number of solvents available for this study. The energy of the NIR bands for $[1]^+$ and $[3]^+$ show very small changes in the three solvents studied (Figures S2 and S4), exemplifying the delocalized nature of these complexes. The NIR band of the Pd complex $[2]^+$ exhibits the largest solvent dependence (Figure S3), shifting to higher energy by 700 cm^{-1} in toluene as compared to CH_3CN . Interestingly, the direction of the shift is opposite to that predicted for solvent polarization contributions to the reorganization energy.⁵¹ Studies have shown that shifts in intervalence band energy can correlate with properties other than dielectric parameters,⁸⁸⁻⁹⁰ and the shift of the NIR band to higher energy for $[2]^+\text{SbF}_6^-$ in toluene could be due to tighter ion association leading to ion pairing and redox asymmetry.^{91,92}

3.5. Theoretical Analysis of the NIR Transitions for $[1]^+$, $[2]^+$, and $[3]^+$

TD-DFT^{76,77} calculations predict correctly the absence of intense transitions for the neutral complexes (**1-3**) in the NIR, and the existence of low energy transitions for the one-electron oxidized derivatives $[1-3]^+$ (Table 7 and Figure S5). The predicted NIR transitions are blue-shifted slightly in comparison to the experimental bands, but exhibit the correct intensity ratio. Analysis of the predicted NIR transitions in terms of the molecular orbitals involved, allows for the assignment of the two NIR bands as LLCT transitions. The predicted higher energy NIR band for each derivative is predominantly a $\beta\text{HOMO}-2 \rightarrow \beta\text{LUMO}$ transition (Figure 9). Analysis of the compositions of the MOs (Tables S1-S3) shows that significant electron density is transferred from the phenolate/phenoxy ring systems to the coordination sphere oxygen atoms.⁷³

The principal calculated electronic excitation that contributes to the intense low-energy NIR band is a $\beta\text{HOMO} \rightarrow \beta\text{LUMO}$ transition (Table 7, Figure 9). For each oxidized derivative $[1-3]^+$ both the donor (βHOMO) and acceptor (βLUMO) orbitals are delocalized π orbitals based primarily on the salen ligand (Figure 9). The metal d_{xz} orbital contribution to the βLUMO increases in the order Pd (9 %) < Ni (12 %) < Pt (17 %). The theoretical calculations predict that the low energy absorption bands for $[1-3]^+$ are delocalized ligand radical transitions.

4. Discussion

The interaction between non-innocent ligands and redox-active transition metals has benefited greatly from both experimental and theoretical analysis to effectively describe the electronic structure of the resulting complexes. Our interest in tetradentate salen ligands is strongly motivated by their versatility as catalysts for important organic transformations,³⁶⁻⁴⁰ and the possibility that ligand oxidation may be operative in the catalytic cycles of such complexes. One-electron oxidation of group 10 metal salens (Ni, Pd, Pt) results in the formation of ligand radical species, with the stability highly dependent on the phenolate substitution as well as on the central metal ion.¹⁷⁻²¹ Experimental and computational studies of the geometric and

electronic structure of $[1]^+$ show that this complex is a delocalized ligand radical species.¹⁹ This analysis, and in particular the investigation of the NIR absorption bands, has led to the assignment of $[1]^+$ as a Class III delocalized mixed valence complex.⁴⁸ We have now extended this study to include the Pd and Pt derivatives to better understand the influence of the central metal ion in mediating the coupling between the two redox-active phenolates, and how this affects the electronic structure and stability of the complexes.

The synthesis of the neutral group 10 metal salens followed established procedures,^{19,21} though only the Pt complex of **H₂Salen** could be obtained in suitable purity. Oxidation of the neutral Pd (**2**) and Pt (**3**) species in CH₂Cl₂ solution results in significant color changes, and X-ray quality crystals of the one-electron oxidized forms were accessible. The structure of the Pt complex $[3]^+$ shows clearly a coordination sphere contraction upon oxidation, which is reproduced by DFT calculations (Table 2). This contraction coincides with that previously reported for $[1]^+$,¹⁹ which was shown by electron charge decomposition analysis (ECDA) calculations to be a result of an increase in both L → M donation and M → L back-donation. ECDA analysis of the Cu derivative $[CuSalcn]^+$ ²² shows that L → M donation increases substantially in comparison to the neutral form, consistent with its formulation as a Cu(III) complex. These results underscore the differences in bonding associated with metal-based as opposed to ligand-based oxidation in the salen systems. Our computational results predict considerable spin density (16.5 %) on Pt in the oxidized form, and this is apparent from the metal *d_{xz}* contribution to the spin density plot (Figure 6). XAS and EPR measurements of $[3]^+$ are consistent with the calculated Pt spin density.²¹

In contrast to $[1]^+$ and $[3]^+$, the X-ray structure of $[2]^+$ displays an asymmetric metal coordination environment, consistent with partial localization of the ligand radical on one of the two phenolates. While the Pd-N bonds decrease upon oxidation, the Pd-O bonds become asymmetric (1.963 Å and 2.003 Å) and lengthen slightly on average (Figure 5, Table 2). The asymmetry is also apparent in the C-O bonds (1.317 Å and 1.263 Å), with the shorter C-O bond on the same side of the molecule as the longer Pd-O bond (Figure 5). This bonding pattern matches with the structures of other reported phenoxyl radical complexes,⁸²⁻⁸⁴ reflecting the diminished electron-donating ability of the phenoxyl ligand relative to that of phenolate. We cannot rule out that crystal packing effects result in the structural asymmetry observed in the solid state structure of $[2]^+$. The calculated coordination sphere bond distances for **2** and $[2]^+$ match the X-ray structures to 0.04 Å (Table 2). While the calculations predict correctly the slight contraction in Pd-N bond lengths upon oxidation, they do not predict the asymmetric Pd-O bonds observed experimentally. This result is presumably due to the propensity of DFT calculations to overemphasize delocalized, higher symmetry structures.⁸⁵ The change in the experimental Pd-O bond lengths upon oxidation differs from the observed contraction of the M-O bonds for the Ni and Pt analogues upon oxidation, and is likely a geometric consequence of diminished delocalization of the ligand radical in $[2]^+$.

In order to assess the degree of electronic coupling between the redox-active phenolates in $[1]^+$, $[2]^+$, and $[3]^+$, and thus the delocalization in the one-electron oxidized forms, the difference between the first and second redox potentials were measured by cyclic voltammetry (CV). At room temperature, the dicationic forms were unstable on the electrochemical time-scale, but stable at 230 K (Figure 7). At this temperature two reversible redox couples were observed, and the difference (ΔE_{ox}) was used as a measure of the electronic coupling in the one-electron oxidized forms; in the absence of electronic coupling, the two redox-active ligands in a symmetric complex undergo oxidation at approximately the same potential.^{18,55} The ΔE_{ox} values follow the trend Pd < Ni < Pt, showing that the Pt complex exhibits the largest coupling between the redox-active phenolates, and the Pd complex the least coupling (Table 3). Based on the electrochemical results, the degree of delocalization increases from Pd < Ni < Pt for the one-electron oxidized forms.

The electronic spectra of $[1]^+$, $[2]^+$, and $[3]^+$ display intense NIR bands, consistent with the formation of ligand radical species (Figure 8).^{9,11,93,94} Investigation of the low energy NIR transitions allows for further analysis of the degree of electronic coupling, and thus delocalization, in the oxidized complexes. A Hush analysis (Equation 4)⁵⁰ of the low energy bands demonstrated that the experimental bandwidths ($\Delta \nu_{1/2}$) for all the oxidized complexes are significantly less than the predicted minimum bandwidth ($\Delta \nu_{\text{HTL}}$) at the high temperature limit (Table 5). Based on the measured $\Delta \nu_{1/2}$ values, and comparison to $\Delta \nu_{\text{HTL}}$, the three oxidized complexes are assigned as borderline Class II/III or Class III mixed valence complexes.⁹⁵ The low energy NIR band of $[2]^+$ displays the largest $\Delta \nu_{1/2}$ value and sensitivity of ν_{max} to solvent variation. Solvent dependence of the IVCT band coincides with valence localization. Interestingly, the shift of the ν_{max} for $[2]^+$ to higher energy in low polarity solvents is opposite to that predicted by the dielectric continuum model for valence localized systems.^{51,96} Enhanced ion-pairing of $[2]^+$ SbF_6^- in non-polar solvents may play a role in the observed solvatochromism.^{91,92} Further investigation of the solvatochromism of the NIR band for $[2]^+$ is impeded by the instability of this complex in many solvents, and the low energy of the transition; solvent transitions at low energy complicate accurate measurement of ν_{max} . Analysis of the NIR bands for the one-electron oxidized derivatives $[1-3]^+$ suggests that the Pd derivative $[2]^+$ is the least delocalized of the series, in agreement with the electrochemical results.

The energy of the intense NIR transition for $[1-3]^+$ is dependent on the relative energies of the donor and acceptor orbitals involved in the transition. TD-DFT analysis predicts that the NIR band is predominantly a $\beta\text{HOMO} \rightarrow \beta\text{LUMO}$ transition for the three one-electron oxidized species (Table 7). As the βHOMO donor orbital is ligand-based, little variation in the energy of this orbital occurs across the series. Similar to the dithiolenes,^{9,11} the energy of the βLUMO is dependent on the interaction of the metal d_{xz} orbital with the appropriate ligand orbital. As this interaction is the antibonding combination, greater overlap raises the energy of the βLUMO resulting in a blue-shift of the IVCT band. Variation of the effective nuclear charge, in combination with relativistic effects, increases the energy of the valence d orbitals in the order $\text{Pd} < \text{Ni} < \text{Pt}$. The predicted energies of the IVCT bands reflect this result, in agreement with the experimental results (Table 7). Overlap between the metal d_{xz} orbital⁹⁷ and the appropriate ligand MO has a direct influence on the electronic coupling between the redox active phenolates, providing a pathway for exchange through the central metal ion. Increased overlap in the order $\text{Pd} < \text{Ni} < \text{Pt}$ is manifest in the degree of delocalization observed experimentally in the one-electron oxidized forms.

5. Summary

We have shown in this work that group 10 metal salen complexes (**1-3**) exist as ligand radical species in their one-electron oxidized forms $[1-3]^+$, all with a high degree of delocalization, yet modulated by the nature of the metal ion. Oxidation results in a symmetrically contracted coordination sphere for $[1]^+$ and $[3]^+$ in the solid state, while $[2]^+$ exhibits a non-symmetric metal coordination environment suggestive that $[2]^+$ is the least delocalized of the series. In solution, (**1-3**) display highly coupled ligand-based oxidation waves and low energy NIR bands consistent with a classification as borderline Class II/III or Class III mixed valence complexes. Analysis of the experimental data, in conjunction with DFT calculations, has provided insight into the degree of delocalization in this series of compounds, as well as the relative energies of the NIR bands. Both the one-electron oxidized Ni and Pt derivatives can be described as Class III mixed valence systems, which is allowed through metal-mediated mixing of the redox-active orbitals on the phenolate ligands. Experimental analysis of the oxidized Pd analogue demonstrates that this derivative is the least delocalized within the series, and is better described as a borderline Class II/III mixed valence complex. The energy match between the Pd d_{xz} orbital and the appropriate ligand MO is less optimal, leading to less overlap through the central

metal ion. Interestingly, it is the oxidized Pd complex that is the least stable within the series,²¹ highlighting the stabilizing effect of delocalization in these systems. Further studies on this and other metal–organic radical species are in progress.

Supplementary Material

Refer to Web version on PubMed Central for supplementary material.

Acknowledgments

This work was supported by a Grant-in-Aid for Scientific Research (No. 17750055 to Y. S.) from the Ministry of Education, Culture, Sports, Science, and Technology of Japan, the NIH (GM-50730 to T. D. P. S.), and Simon Fraser University start-up funds (T. S.). WestGrid is thanked for access to computational resources.

References

1. Rogers MS, Dooley DM. *Curr Opin Chem Biol* 2003;7:189. [PubMed: 12714051]
2. Stubbe J, van der Donk WA. *Chem Rev* 1998;98:705. [PubMed: 11848913]
3. Whittaker JW. *Metal Ions Biol Sys* 1994;30:315.
4. Whittaker JW. *Chem Rev* 2003;103:2347. [PubMed: 12797833]
5. Hendrickson DN, Pierpont CG. *Top Curr Chem* 2004;234:63.
6. Pierpont CG. *Coord Chem Rev* 2001;216:99.
7. Pierpont CG. *Coord Chem Rev* 2001;219:415.
8. Kaim W, Schwederski B. *Pure Appl Chem* 2004;76:351.
9. Ray K, Petrenko T, Wieghardt K, Neese F. *Dalton Trans* 2007:1552. [PubMed: 17426855]
10. Ray K, George SD, Solomon EI, Wieghardt K, Neese F. *Chem Eur J* 2007;13:2783.
11. Ray K, Weyhermuller T, Neese F, Wieghardt K. *Inorg Chem* 2005;44:5345. [PubMed: 16022533]
12. Mederos A, Dominguez S, Hernandez-Molina R, Sanchiz J, Brito F. *Coord Chem Rev* 1999;195:913.
13. Peng SM, Chen CT, Liaw DS, Chen CI, Yu W. *Inorg Chim Acta* 1985;101:L31.
14. Bachler V, Olbrich G, Neese F, Wieghardt K. *Inorg Chem* 2002;41:4179. [PubMed: 12160406]
15. Herebian D, Bothe E, Neese F, Weyhermueller T, Weighardt K. *J Am Chem Soc* 2003;125:9116. [PubMed: 15369369]
16. Benisvy L, Kannappan R, Song YF, Milikisyants S, Huber M, Mutikainen I, Turpeinen U, Garnez P, Bernasconi L, Baerends EJ, Hartl F, Reedijk J. *Eur J Inorg Chem* 2007:631.
17. Rotthaus O, Jarjays O, Thomas F, Philouze C, Del Valle CP, Saint-Aman E, Pierre JL. *Chem Eur J* 2006;12:2293.
18. Rotthaus O, Thomas F, Jarjays O, Philouze C, Saint-Aman E, Pierre JL. *Chem Eur J* 2006;12:6953.
19. Storr T, Wasinger EC, Pratt RC, Stack TDP. *Angew Chem Int Ed* 2007;46:5198.
20. Rotthaus O, Jarjays O, Del Valle CP, Philouze C, Thomas F. *Chem Comm* 2007:4462. [PubMed: 17971956]
21. Shimazaki Y, Yajima T, Tani F, Karasawa S, Fukui K, Naruta Y, Yamauchi O. *J Am Chem Soc* 2007;129:2559. [PubMed: 17290991]
22. Storr T, Verma P, Pratt RC, Wasinger EC, Shimazaki Y, Stack TDP. *J Am Chem Soc* 2008;130:15448. [PubMed: 18939830]
23. Blackmore KJ, Lal N, Ziller JW, Heyduk AF. *J Am Chem Soc* 2008;130:2728. [PubMed: 18266370]
24. Buttner T, Geier J, Frison G, Harmer J, Calle C, Schweiger A, Schonberg H, Grutzmacher H. *Science* 2005;307:235. [PubMed: 15653498]
25. Haneline MR, Heyduk AF. *J Am Chem Soc* 2006;128:8410. [PubMed: 16802801]
26. Konigsmann M, Donati N, Stein D, Schonberg H, Harmer J, Sreekanth A, Grutzmacher H. *Angew Chem Int Ed* 2007;46:3567.
27. Maire P, Konigsmann M, Sreekanth A, Harmer J, Schweiger A, Grutzmacher H. *J Am Chem Soc* 2006;128:6578. [PubMed: 16704256]

28. Miyazato Y, Wada T, Tanaka K. *Bull Chem Soc Jpn* 2006;79:745.
29. Ringenberg MR, Kokatam SL, Heiden ZM, Rauchfuss TB. *J Am Chem Soc* 2008;130:788. [PubMed: 18163627]
30. Adhikari D, Mossin S, Basuli F, Huffman JC, Szilagyi RK, Meyer K, Mindiola DJ. *J Am Chem Soc* 2008;130:3676. [PubMed: 18302384]
31. Wang YD, DuBois JL, Hedman B, Hodgson KO, Stack TDP. *Science* 1998;279:537. [PubMed: 9438841]
32. Chaudhuri P, Hess M, Florke U, Wieghardt K. *Angew Chem Int Ed* 1998;37:2217.
33. Archer AM, Bouwkamp MW, Cortez MP, Lobkovsky E, Chirik PJ. *Organometallics* 2006;25:4269.
34. Bart SC, Lobkovsky E, Bill E, Chirik PJ. *J Am Chem Soc* 2006;128:5302. [PubMed: 16620076]
35. Russell SK, Lobkovsky E, Chirik PJ. *J Am Chem Soc* 2009;131:36. [PubMed: 19128168]
36. Canali L, Sherrington DC. *Chem Soc Rev* 1999;28:85.
37. Darensbourg DJ. *Chem Rev* 2007;107:2388. [PubMed: 17447821]
38. McGarrigle EM, Gilheany DG. *Chem Rev* 2005;105:1563. [PubMed: 15884784]
39. Baleizao C, Garcia H. *Chem Rev* 2006;106:3987. [PubMed: 16967927]
40. Gupta KC, Sutar AK. *Coord Chem Rev* 2008;252:1420.
41. Abuelwafa SM, Issa RM, McAuliffe CA. *Inorg Chim Acta* 1985;99:103.
42. Audebert P, Capdevielle P, Maumy M. *New J Chem* 1991;15:235.
43. Bottcher A, Elias H, Jager EG, Langfelderova H, Mazur M, Muller L, Paulus H, Pelikan P, Rudolph M, Valko M. *Inorg Chem* 1993;32:4131.
44. Freire C, deCastro B. *J Chem Soc Dalton Trans* 1998:1491.
45. Pasini A, Bernini E, Scaglia M, DeSantis G. *Polyhedron* 1996;15:4461.
46. Shimazaki Y, Tani F, Fukui K, Naruta Y, Yamauchi O. *J Am Chem Soc* 2003;125:10512. [PubMed: 12940721]
47. Sarangi R, George SD, Rudd DJ, Szilagyi RK, Ribas X, Rovira C, Almeida M, Hodgson KO, Hedman B, Solomon EI. *J Am Chem Soc* 2007;129:2316. [PubMed: 17269767]
48. Robin MB, Day P. *Adv Inorg Chem Radiochem* 1967;10:247.
49. Creutz C, Taube H. *J Am Chem Soc* 1969;91:3988.
50. Hush NS. *Prog Inorg Chem* 1967;8:391.
51. Chen PY, Meyer TJ. *Chem Rev* 1998;98:1439. [PubMed: 11848939]
52. Demadis KD, Hartshorn CM, Meyer TJ. *Chem Rev* 2001;101:2655. [PubMed: 11749392]
53. Brunschwig BS, Creutz C, Sutin N. *Chem Soc Rev* 2002;31:168. [PubMed: 12122642]
54. Nelsen SF. *Chem Eur J* 2000;6:581.
55. D'Alessandro DM, Keene FR. *Chem Soc Rev* 2006;35:424. [PubMed: 16636726]
56. Lu CC, Bill E, Weyhermuller T, Bothe E, Wieghardt K. *J Am Chem Soc* 2008;130:3181. [PubMed: 18284242]
57. Adams DM, Noodleman L, Hendrickson DN. *Inorg Chem* 1997;36:3966.
58. Chang HC, Miyasaka H, Kitagawa S. *Inorg Chem* 2001;40:146. [PubMed: 11195373]
59. Chaudhuri P, Verani CN, Bill E, Bothe E, Weyhermuller T, Wieghardt K. *J Am Chem Soc* 2001;123:2213. [PubMed: 11456867]
60. Nairn A, Bhalla R, Foxon SP, Liu X, Yellowlees LJ, Gilbert BC, Walton PH. *J Chem Soc Dalton Trans* 2002:1253.
61. Dogan A, Sarkar B, Klein A, Lissner F, Schleid T, Fiedler J, Zalis S, Jain VK, Kaim W. *Inorg Chem* 2004;43:5973. [PubMed: 15360246]
62. Ye S, Sarkar B, Lissner F, Schleid T, van Slageren J, Fiedler J, Kaim W. *Angew Chem Int Ed* 2005;44:2103.
63. Fox GA, Pierpont CG. *Inorg Chem* 1992;31:3718.
64. Perrin, DD.; Armarego, WLF. *Purification of Laboratory Chemicals*. Vol. 1. Pergamon Press; New York: 1988.
65. Ibers, JA. *International Tables for X-ray Crystallography*. Vol. IV. Kynoch; Birmingham: 1974.

66. TeXsan. Crystal Structure Analysis Package. Molecular Structure Corporation; 1992.
67. Frisch, MJT., et al. Gaussian 03, Revision C.02. Gaussian, Inc; Wallingford, CT: 2004.
68. Perdew JP, Burke K, Ernzerhof M. Phys Rev Lett 1996;77:3865. [PubMed: 10062328]
69. Fuentealba P, Preuss H, Stoll H, Vonszentpaly L. Chem Phys Lett 1982;89:418.
70. Nicklass A, Dolg M, Stoll H, Preuss H. J Chem Phys 1995;102:8942.
71. Poverenov E, Efremenko I, Frenkel AI, Ben-David Y, Shimon LJW, Leitun G, Konstantinovski L, Martin JML, Milstein D. Nature 2008;455:1093.
72. Schafer A, Horn H, Ahlrichs R. J Chem Phys 1992;97:2571.
73. Gorelsky, SI. AOMix: Program for Molecular Orbital Analysis. University of Ottawa; Canada: 2007. <http://www.sg-chem.net/>
74. Gorelsky SI, Lever ABP. J Organomet Chem 2001;635:187.
75. Gorelsky SI, Solomon EI. Theoretical Chem Acc 2008;119:57.
76. Casida, ME. Recent Advances in Density Functional Methods. Chong, DP., editor. World Scientific; Singapore: 1995. p. 155
77. Stratmann RE, Scuseria GE, Frisch MJ. J Chem Phys 1998;109:8218.
78. Barone V, Cossi M, Tomasi J. J Chem Phys 1997;107:3210.
79. Barone V, Cossi M, Tomasi J. J Comput Chem 1998;19:404.
80. Miertus S, Scrocco E, Tomasi J. Chem Phys 1981;55:117.
81. Tomasi J, Mennucci B, Cances E. J Mol Struct 1999;464:211.
82. Benisvy L, Blake AJ, Collison D, Davies ES, Garner CD, McInnes EJJ, McMaster J, Whittaker G, Wilson C. Chem Comm 2001:1824. [PubMed: 12240333]
83. Benisvy L, Blake AJ, Collison D, Davies ES, Garner CD, McInnes EJJ, McMaster J, Whittaker G, Wilson C. Dalton Trans 2003:1975.
84. Sokolowski A, Bothe E, Bill E, Weyhermuller T, Wieghardt K. Chem Comm 1996:1671.
85. Cramer, CJ. Essentials of Computational Chemistry. Vol. 2. Wiley; West Sussex, England: 2004.
86. Hush NS. Coord Chem Rev 1985;64:135.
87. CRC Handbook of Chemistry and Physics. CRC Press; Boca Raton, FL: 1995.
88. Dinolfo PH, Lee SJ, Coropceanu V, Bredas JL, Hupp JT. Inorg Chem 2005;44:5789. [PubMed: 16060631]
89. Nelsen SF, Konradsson AE, Telo JP. J Am Chem Soc 2005;127:920. [PubMed: 15656630]
90. Lear BJ, Glover SD, Salsman JC, Londergan CH, Kubiak CP. J Am Chem Soc 2007;129:12772. [PubMed: 17902656]
91. Blackbourn RL, Dong YH, Lyon LA, Hupp JT. Inorg Chem 1994;33:4446.
92. Blackbourn RL, Hupp JT. J Phys Chem 1990;94:1788.
93. Herebian D, Bothe E, Neese F, Weyhermuller T, Wieghardt K. J Am Chem Soc 2003;125:9116. [PubMed: 15369369]
94. Herebian D, Wieghardt KE, Neese F. J Am Chem Soc 2003;125:10997. [PubMed: 12952481]
95. The electronic coupling parameter H_{ab} was not calculated in this work due to the inaccuracy in assigning the electron transfer distance (r_{ab}) in the oxidized metal salen complexes.
96. Demadis KD, Hartshorn CM, Meyer TJ. Chem Rev 2001;101:2655. [PubMed: 11749392]
97. A combination of valence ionization potential (IE_2 (kJ/mol); Ni = 1753, Pd = 1875, Pt = 1791) and size of the $M nd$ orbitals influences the d_{xz} character in the β LUMO. In the case of the metal salens d_{xz} character increases in the order Pd < Ni < Pt.

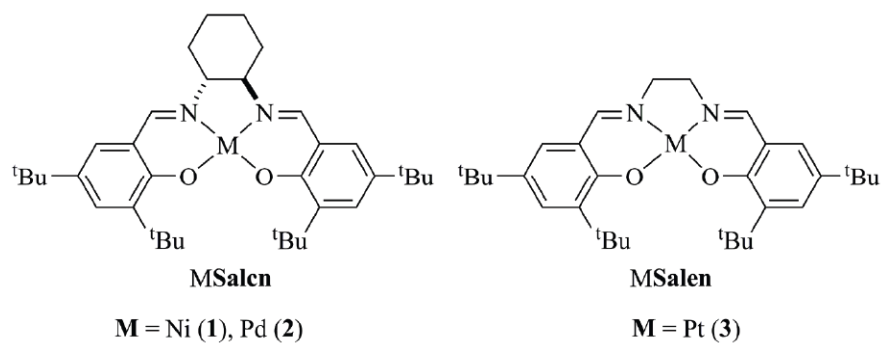


Figure 1.
Structures of the neutral metal salen complexes.

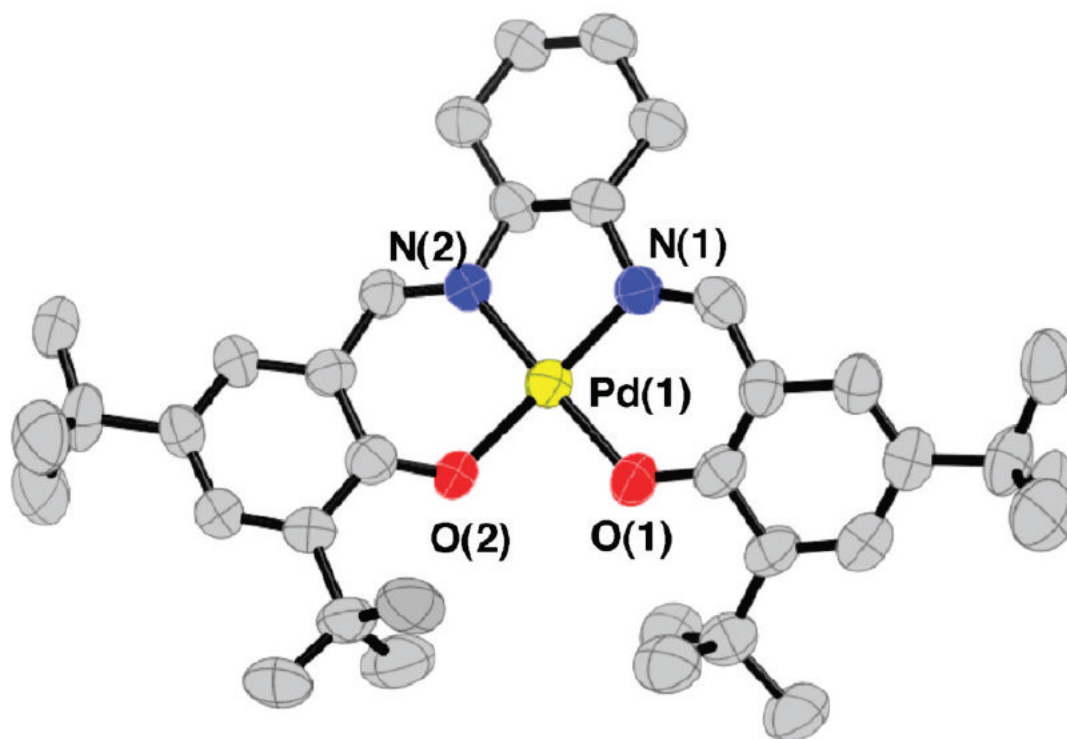


Figure 2.

ORTEP view of one of the two PdSalcn (**2**) molecules in the unit cell. Hydrogen atoms are omitted for clarity. Selected bond lengths (Å) and angles (°); Pd(1)-O(1) 1.970(5), Pd(1)-O(2) 1.969(5), Pd(1)-N(1) 1.959(6), Pd(1)-N(2) 1.949(6), O(1)-C(1) 1.304(9), O(1)-C(16) 1.288(9), O(1)-Pd(1)-O(2) 87.2(2), O(1)-Pd(1)-N(1) 93.9(2), O(1)-Pd(2)-N(2) 176.2(3), O(2)-Pd(1)-N(1) 176.3(3), O(2)-Pd(1)-N(2) 94.5(2), N(1)-Pd(1)-N(2) 84.6(3).

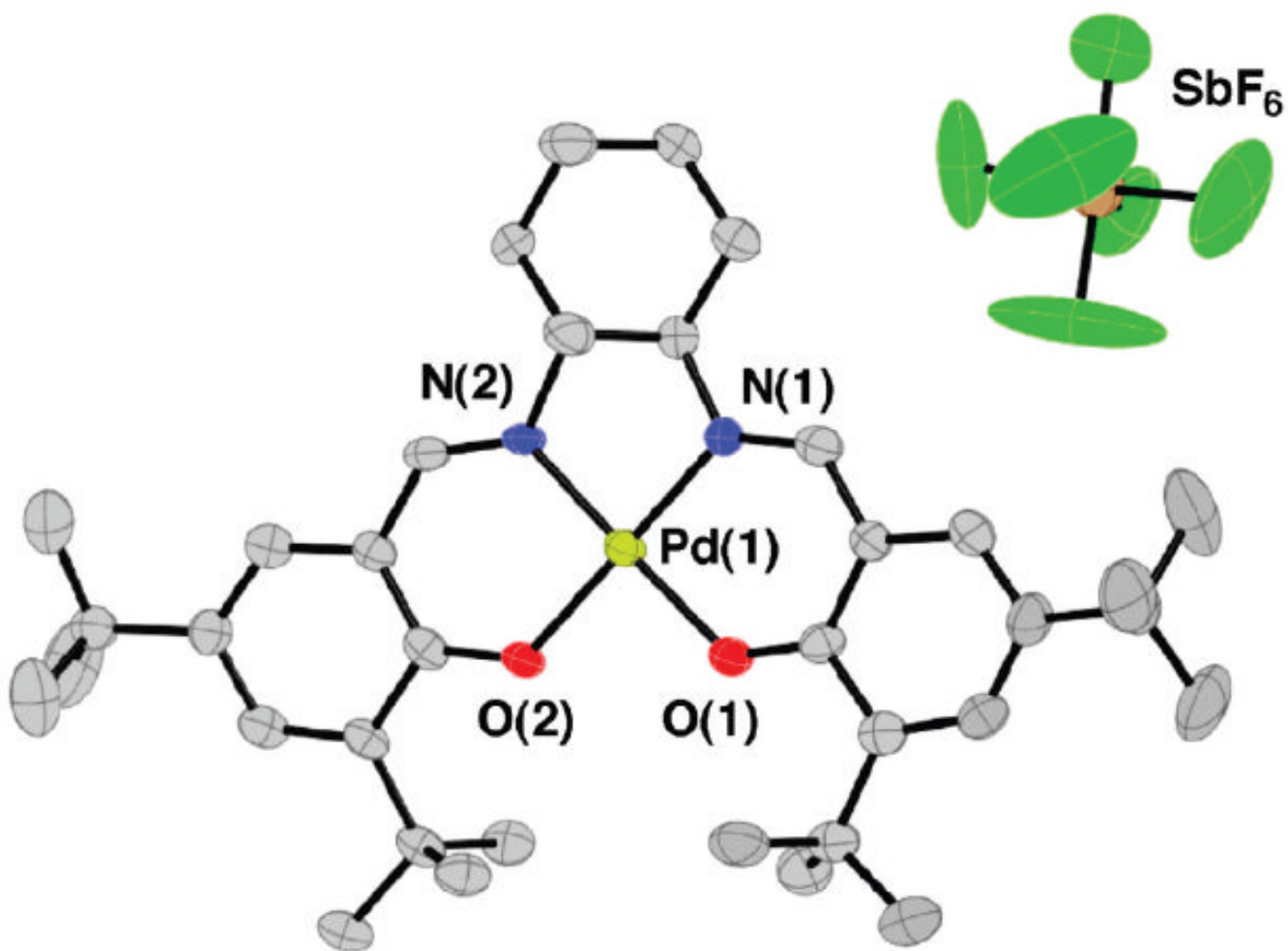


Figure 3.

ORTEP view of $[\text{PdSalcn}]\text{SbF}_6$ $[2]^+$. Hydrogen atoms are omitted clarity. Selected bond lengths (\AA) and angles ($^\circ$); Pd(1)-O(1) 2.003(4), Pd(1)-O(2) 1.963(4), Pd(1)-N(1) 1.943(5), Pd(1)-N(2) 1.942(5), O(1)-C(1) 1.263(7), O(2)-C(16) 1.318(7), O(1)-Pd(1)-O(2) 87.5(2), O(1)-Pd(1)-N(1) 93.2(2), O(1)-Pd(1)-N(2) 176.7(2), O(2)-Pd(1)-N(1) 178.7(2), O(2)-Pd(1)-N(2) 94.5(2), N(1)-Pd(1)-N(2) 84.9(2).

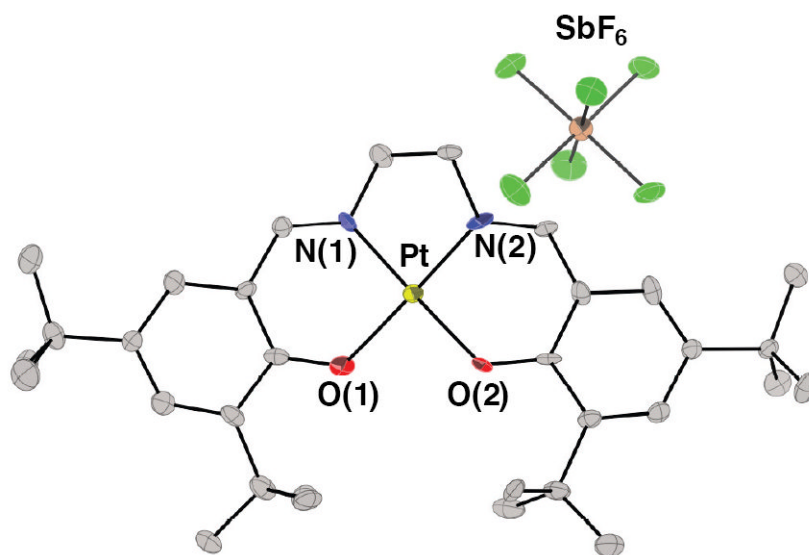
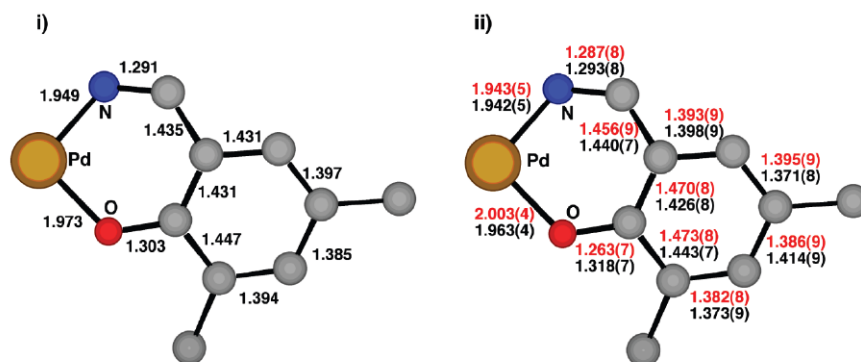
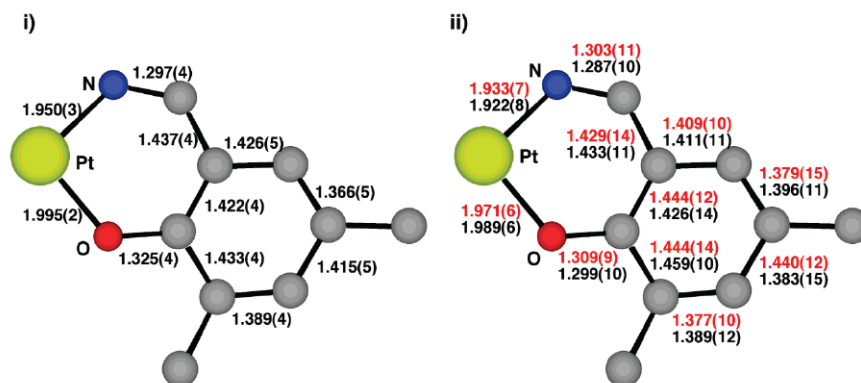


Figure 4. ORTEP view of [PtSalen]SbF₆ [3]⁺. Hydrogen atoms are omitted for clarity. Selected bond lengths (Å) and angles (°); Pt-O(1) 1.971(6), Pt-O(2) 1.989(6), Pt-N(1) 1.933(7), Pt-N(2) 1.922(8), O(1)-C(1) 1.309(9), O(2)-C(12) 1.299(10), O(1)-Pt-O(2) 89.0(2), O(1)-Pt-N(1) 92.5(3), O(1)-Pt-N(2) 178.4(2), O(2)-Pt-N(1) 178.5(2), O(2)-Pt-N(2) 92.6(3), N(1)-Pt-N(2) 85.9(3).

(A) Pd complexes **2** (i) and **[2]⁺** (ii).(B) Pt complexes **3** (i) and **[3]⁺** (ii).**Figure 5.**

Bond length comparison of the neutral and oxidized Pd and Pt complexes: (A) neutral **2** (i) and oxidized **[2]⁺** (ii); (B) neutral **3** (i) and oxidized **[3]⁺** (ii). The bond length values for **2** are an average of the two independent molecules in the unit cell, for **3** the two phenolate moieties are related by a C_2 axis.

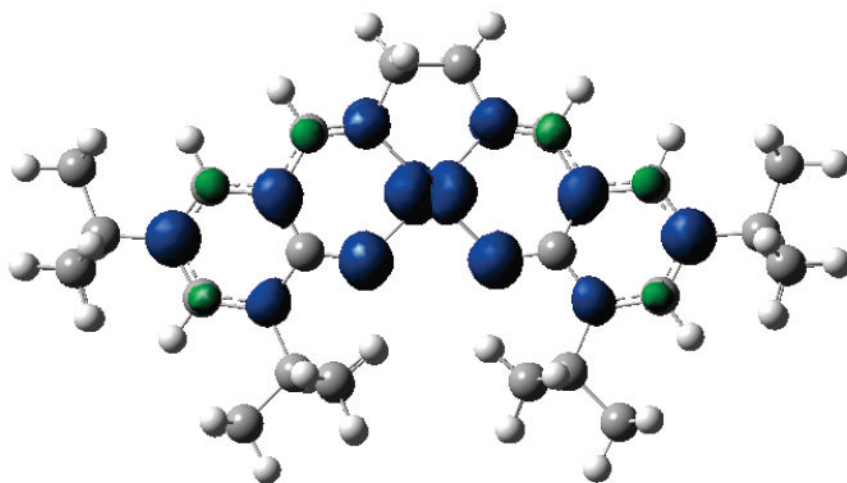


Figure 6. Calculated spin density for $[3]^+$ showing delocalization over the ligand framework with ca. 17 % occupancy on Pt (d_{xz}).

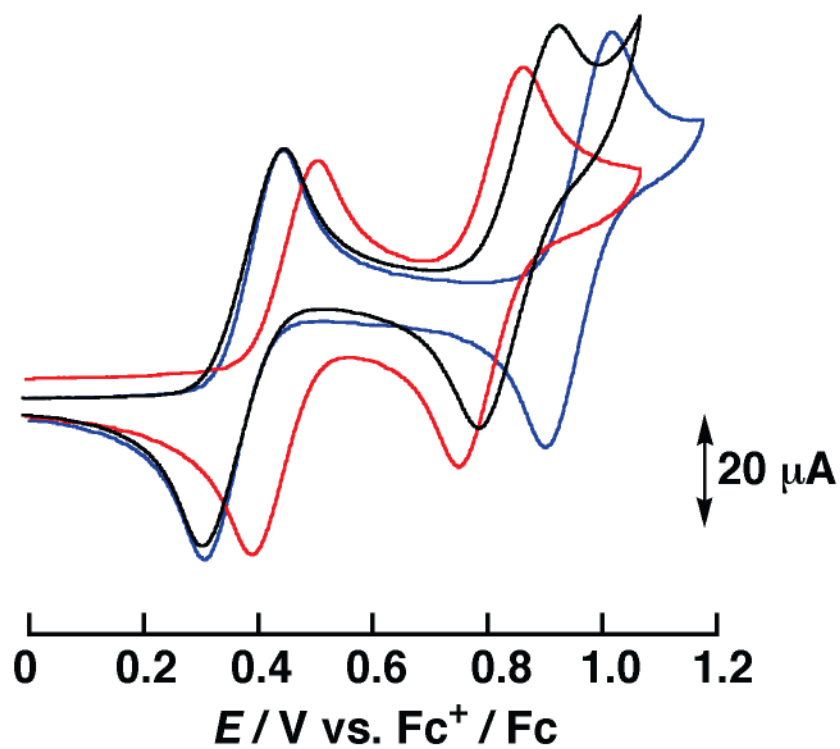
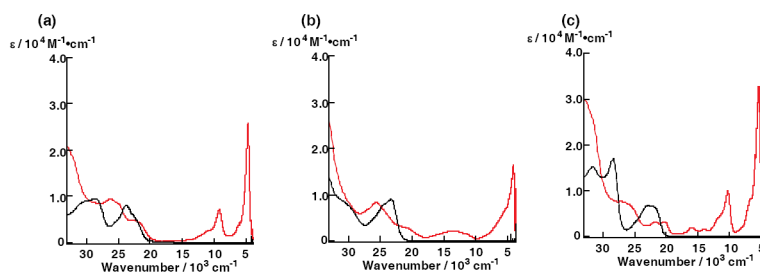


Figure 7. Cyclic voltammograms (vs. Fc^+/Fc) of **1** (black), **2** (red), and **3** (blue). Conditions; 1mM complex, 0.1M TBAP, scan rate 100mV/s, CH_2Cl_2 , 230 K.

**Figure 8.**

Absorption spectra of the neutral (black) and one-electron oxidized (red) group 10 metal salen complexes: (a) **1** and $[\mathbf{1}]^+$, (b) **2** and $[\mathbf{2}]^+$, (c) **3** and $[\mathbf{3}]^+$. Conditions; 0.1 mM complex, CH_2Cl_2 , 298 K.

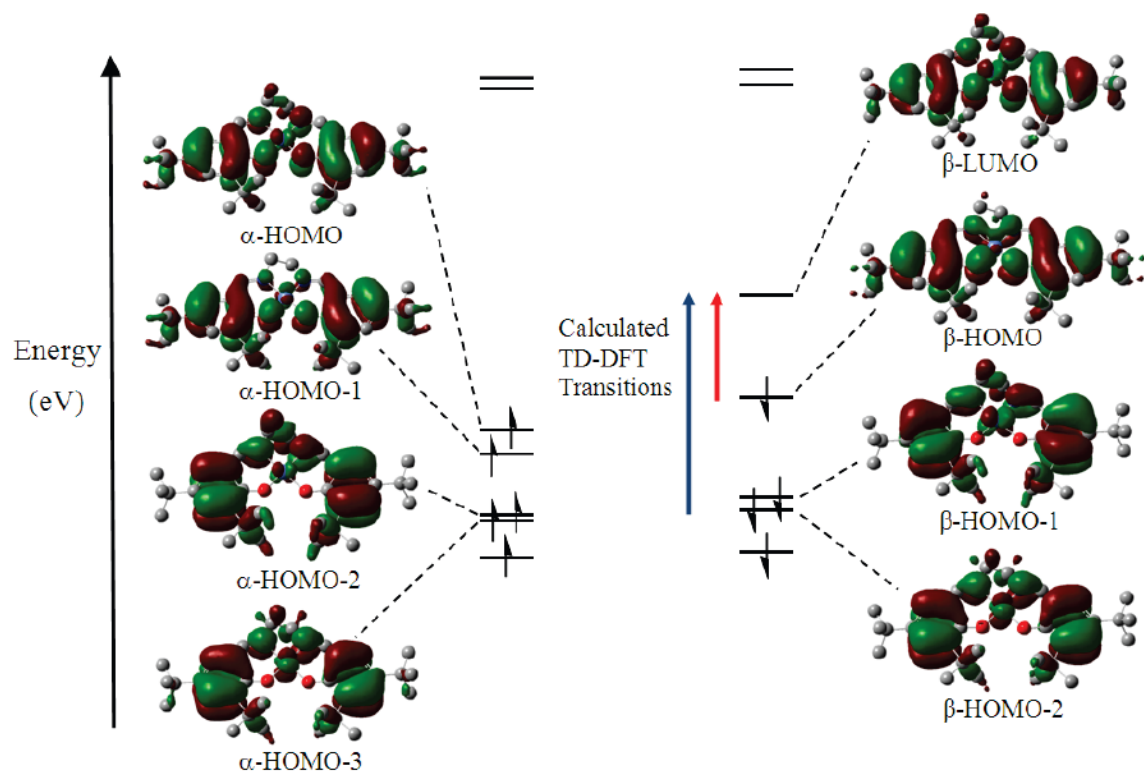


Figure 9.

Kohn-Sham molecular orbital diagram of $[1]^+$ and TD-DFT assignment of the calculated NIR transitions at 11100 cm^{-1} (blue arrow; β -HOMO-2 \rightarrow β -LUMO) and 5100 cm^{-1} (red arrow; β -HOMO \rightarrow β -LUMO). The predicted electronic transitions in $[2]^+$ and $[3]^+$ are similar.

Table 1

Crystal data for [2], [2]⁺ and [3]⁺.

Crystal Data	[2]	[2] ⁺	[3] ⁺
Formula	C ₃₆ H ₅₂ N ₂ O ₂ Pd	C ₃₆ H ₅₂ F ₆ N ₂ O ₂ PdSb	C ₃₃ H ₄₈ Cl ₂ F ₆ N ₂ O ₂ PtSb
fw	651.22	886.98	1006.49
crystal system, space group	Orthorhombic, P2 ₁ 2 ₁ 2 ₁	Monoclinic, P2 ₁ /a	Triclinic, P-1
a (Å)	10.1770(9)	11.8995(3)	11.414(5)
b (Å)	26.269(3)	17.6082(5)	15.075(7)
c (Å)	26.925(3)	18.8645(5)	15.294(8)
α (deg)	—	—	123.04(3)
β (deg)	—	101.3523(8)	89.59(4)
γ (deg)	—	—	112.12(4)
V [Å ³]	7198(4)	3875.3(2)	1976(4)
Z, D _{calc} [g/cm ³]	8, 1.202	4, 1.453	2, 1.691
μ(MoKα) [cm ⁻¹]	5.46	7.73	43.97
Temperature (K)	130	130	130
θ _{min-max}	3.0, 27.5	3.0, 27.5	3.1, 27.5
reflens colld/unique	16446, 740	24056, 433	8895, 424
Residuals (R ² , all data)	0.1680	0.1591	0.2086
Residuals (R, I>2σ (I))	0.0531	0.0608	0.0683

Table 2

Experimental and Calculated (in Parentheses) Coordination Sphere Metrical Parameters for the Complexes in Å.

Complex	M-O1	M-O2	M-N1	M-N2
1 ^a	1.856 ^d (1.858 ^e)		1.861 ^d (1.852 ^e)	
[1] ^{+b}	1.827 (1.844 ^e)	1.830	1.825 (1.841 ^e)	1.843
2	1.973 ^d (2.007 ^e)		1.950 ^d (1.963 ^e)	
[2] ⁺	1.963 (1.995 ^e)	2.003	1.942 (1.953 ^e)	1.942
3 ^c	1.995 (2.017 ^e)		1.949 (1.962 ^e)	
[3] ⁺	1.971 (1.997 ^e)	1.989	1.933 (1.951 ^e)	1.922

^a Metrical data from reference [46].

^b Metrical data from reference [19].

^c Metrical data from reference [21].

^d Average of the two molecules in the unit cell.

^e Optimization results in a C₂-symmetric structure. See experimental section for details.

Table 3

Redox potentials for **1**, **2**, and **3** versus Fc^+/Fc (1mM complex, 0.1M TBAP, scan rate 100mV/s, CH_2Cl_2 , 230 K), and the comproportionation constant (K_c) at 230 K.

Compound	$E_{1/2}^1$ (mV)	$E_{1/2}^2$ (mV)	$\Delta E_{\text{ox}} (E_{1/2}^2 - E_{1/2}^1)$ (mV)	K_c (M^{-1})
1	370	850	480	3.29×10^{10}
2	450	800	350	4.66×10^7
3	350	940	590	8.45×10^{12}

Table 4Electronic Properties of the Complexes. Conditions; 0.1 mM complex, CH₂Cl₂, 298 K.

Complex	$\lambda_{\text{max}}, \text{cm}^{-1}$ ($\epsilon \times 10^3, \text{M}^{-1} \text{cm}^{-1}$)
1 ^a	23700 (9.4), 22500 sh (6.5), 18000 br (0.4)
[1] ^{+a}	26000 (9.4), 25000 sh (8.4), 22000 (4.6), 11300 (2.2), 9150 (7.2), 4700 (25.6)
2	31000 sh (8.8), 24800 (7.3), 23400 (9.0)
[2] ⁺	25600 (8.4), 21000 sh (32.9), 13500 (2.2), 4100 (16.4)
3 ^b	31750 (7.7), 28490 (9.2), 23150 (3.3), 21900 (3.0)
[3] ⁺	26000 sh (7.0), 21700 (3.2), 20300 (3.2), 16000 (1.9), 14000 (1.6), 10300 (9.4), 5450 (32.6)

^a As previously reported^[19].^b As previously reported^[21].

Table 5

Band shape parameters for the low energy NIR transition of [1]⁺, [2]⁺, and [3]⁺.

Compound	ν_{\max} (cm ⁻¹)	ϵ (M ⁻¹ cm ⁻¹)	$\Delta\nu_{1/2}$ (cm ⁻¹)	$\Delta\nu_{\text{HTL}}$ (cm ⁻¹) ^a	% $\Delta\nu_{\text{HTL}}$ ^b
[1] ⁺	4700	25600	670	3300	20 %
[2] ⁺	4100	16400	1430	3080	46 %
[3] ⁺	5450	32600	970	3550	27 %

^a From equation 4, 50.86

^b $\Delta\nu_{1/2} / \Delta\nu_{\text{HTL}} \times 100 \%$

Table 6The effect of solvent polarity on the NIR band energy for $[1]^+$, $[2]^+$, and $[3]^+$.

Solvent	Dielectric parameter $(1/\eta^2 - 1/\epsilon_s)^a$	$\nu_{\max} [1]^+ (\text{cm}^{-1})$	$\nu_{\max} [2]^+ (\text{cm}^{-1})$	$\nu_{\max} [3]^+ (\text{cm}^{-1})$
toluene	0.026	4880	4900	5470
CH ₂ Cl ₂	0.382	4700	4100	5450
CH ₃ CN	0.528	4750	4200	5540

^a Calculated from [87], where η and ϵ_s are the optical and static dielectric constants of the medium.

Table 7

Comparison of the experimental and predicted TD-DFT NIR transitions for [1]⁺, [2]⁺, and [3]⁺.

Complex	Transition (MO number) ^a	Energy (cm ⁻¹) expt	Energy (cm ⁻¹) calcd	Oscillator strength (predicted)	Assignment ^b
[1] ⁺	βHOMO-2 → βLUMO	9200	11100	0.045	LLCT
	βHOMO → βLUMO	4700	5100	0.231	LLCT
[2] ⁺	βHOMO-2 → βLUMO	13800	12300	0.031	LLCT
	βHOMO → βLUMO	4100	4700	0.239	LLCT
[3] ⁺	βHOMO-2 → βLUMO	10300	11500	0.047	LLCT
	βHOMO → βLUMO	5450	6200	0.242	LLCT

^aTD-DFT (30 states); PBE0 / SDDAll (Ni, Pd, Pt) / TZVP (C, H, O, N).

^bAssignment by AOMIX decomposition of relevant MOs into constituent components.^{73,74}